A Fully Integrated Electrostatic Charge Boosting Rectifier for Triboelectric Energy Harvesting

Peng, Wenyu; Yue, Xinling; Van Driel, Willem D.; Zhang, Guoqi; Du, Sijun

DOI
10.1109/JSSC.2024.3479072

Publication date
2024

Document Version
Final published version

Published in
IEEE Journal of Solid-State Circuits

A Fully Integrated Electrostatic Charge Boosting Rectifier for Triboelectric Energy Harvesting

Wenyu Peng, *Graduate Student Member, IEEE*, Xinling Yue, *Graduate Student Member, IEEE*, Willem D. van Driel, Guoqi Zhang, *Fellow, IEEE*, and Sijun Du, *Senior Member, IEEE*

***Abstract*— The various application scenarios of triboelectric nanogenerator (TENG) have attracted increasing research interest, while one of the biggest challenges is the energy extraction efficiency. Due to the small and time-varying inherent capacitor in a TENG, the previous energy extraction techniques e.g., full-bridge rectifier (FBR) and bias-flip (BF) rectifier, performed not well. To extract more energy from TENG, this article proposed a fully integrated switched-capacitor (SC) rectifier with an electrostatic charge boosting (ECB) technique, achieving simultaneous extraction from the synchronized triboelectric energy and self-excited electrostatic energy. The proposed rectifier was fabricated in a 180-nm BCD process. With the proposed ECB technique, the theoretical analysis and measurements show a quadratically increasing output power with respect to the rectification voltage, attaining a constant maximum power point (MPP) at the breakdown voltage of the circuit. A maximum output power of 127.6 μW is measured with a TENG fabricated in-house. Compared to a passive FBR, the proposed rectifier enhances the output power by 14 times.**

***Index Terms*— Energy harvesting, maximum power point tracking (MPPT), power management, rectifier, switched-capacitor (SC) converter, synchronous switching, triboelectric nanogenerator (TENG).**

I. Introduction

ENERGY is essential to all electronic devices. In the past decades, the Internet-of-Things (IoT) has been dramatically developed with an exponentially increasing number of IoT-connected devices. Currently, most IoT devices are powered by batteries. Despite their high power density, they will run out of energy eventually, while replacing and recharging these batteries are very impractical due to the ubiquitously implemented IoT devices. Besides, they suffer from poor sustainability and cause severe pollution to the environment. To address these issues, energy harvesting techniques that convert sustainable ambient energy into electrical energy have gained many research interests and are considered sustainable and environment-friendly power solutions. Amongst various energy sources in the environment, mechanical/kinetic energy is one that exists almost everywhere. In recent years, a new mechanical–electrical energy transducer, triboelectric nanogenerator (TENG), was proposed and drew much interest due to its flexibility and high power density [1]. Compared to traditional mechanical energy transducers, such as piezoelectric, electromagnetic, and electrostatic transducers, TENG gains advantages in self-powering and capability in harvesting both regular and irregular mechanical energy, such as human movement [2], [3], tides [4], wind [5], and ultrasound [6], [7].

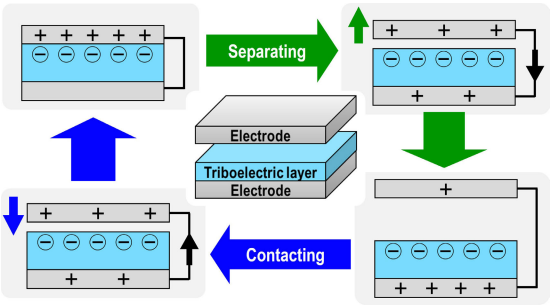

Fig. 1. Structure and operation mechanism of a typical contact-separation TENG.

A TENG transduces mechanical energy into electrical energy via triboelectric effect and electrostatic induction [8]. A typical type of TENG used to harvest energy from reciprocating motion is the vertical contact-separation TENG. Fig. 1 illustrates the structure and operation mechanism. The contact-separation TENG usually contains two electrodes and at least one insulating triboelectric layer. The two electrodes form a capacitor, C_T, which varies when the electrodes are moving away from or forward to each other. Meanwhile, the static surface charge on the triboelectric layer, generated via contact due to the triboelectric effect, forms displacement current during movement and thus induces current flowing between the electrodes, which can be equivalently converted into an ac current source, I_T, connected in parallel with C_T.

To utilize triboelectric energy and provide a dc supply to load electronics, rectifiers are typically required. A full-bridge rectifier (FBR) was widely employed to extract energy from TENGs, with its topology and waveform illustrated in Fig. 2(a) [9], [10]. Despite its simplicity, it sets a high voltage threshold, only allowing it to extract energy when the voltage across TENG (V_T) is higher than the rectifier output voltage (V_{REC}). When V_{REC} is high, a large amount of energy is wasted to charge or discharge C_T periodically. Another passive rectifier, the dual-output rectifier (DOR), was proposed with two separate V_{REC} to tackle the asymmetric outputs of TENG; however, it still suffers from the self-charging

Received 22 July 2024; revised 18 September 2024; accepted 7 October 2024. Date of publication 23 October 2024; date of current version 29 May 2025. This article was approved by Associate Editor Chulwoo Kim. *(Corresponding author: Sijun Du.)*

The authors are with the Department of Microelectronics, Delft University of Technology, 2628 CD Delft, The Netherlands (e-mail: sijun.du@tudelft.nl).

Color versions of one or more figures in this article are available at https://doi.org/10.1109/JSSC.2024.3479072.

Digital Object Identifier 10.1109/JSSC.2024.3479072

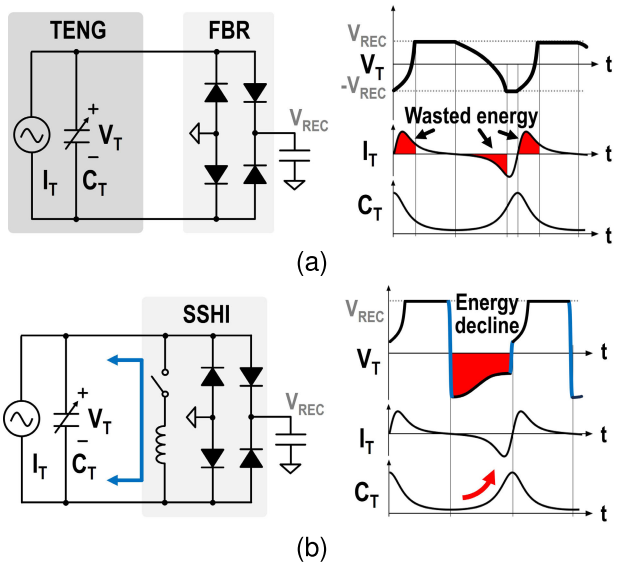

Fig. 2. Topology and waveform of conventional works. (a) FBR and (b) SSHI rectifier.

and discharging loss [11], [12], [13], [14]. Furthermore, half-bridge rectifier [15] and Bennet's doubler [16], [17] achieve better output performance by eliminating the discharging loss when V_T is negative but meanwhile sacrifice the energy which could have been harvested during negative-V_T semi-period.

The solution to tackle this issue is to employ active rectifiers, which detect the state of TENG and operate synchronously [18]. The synchronized switch harvesting on inductor (SSHI) technique, shown in Fig. 2(b), was employed in triboelectric energy harvesting to flip the voltage across C_T via an inductor when I_T crosses zero [19]. This technique reduces the energy wasted to flip and build up V_T; however, a decline of $|V_T|$ can be observed during the negative-V_T semi-period due to the increasing C_T, which indicates a loss of electrostatic energy [20]. In contrast, energy harvesters with constant intrinsic capacitance, like piezoelectric harvesters or some TENGs, will not suffer from voltage decline when the SSHI technique is employed [21], [22]. For instance, a multichip-stacked bias-flip (MSC-BF) rectifier was proposed to extract more triboelectric energy at a higher V_{REC} voltage from a wind-driven TENG that has a constant C_T [21]. It achieves promising performance with two stacked chips; however, it was designed for TENGs with a constant C_T. Another shortcoming of the SSHI technique is that a bulky inductor is needed to achieve a high-voltage flipping efficiency. In comparison, the synchronous switch harvesting on capacitor (SSHC) rectifier is more advantageous in reducing the system form factor [23], [24], [25], [26]. Besides, thanks to the small C_T, small flipping capacitors (<1 nF) will be sufficient to realize a high flipping efficiency, which allows the rectifier to be integrated on chip.

In this work, we propose a fully integrated switched-capacitor (SC) rectifier with an electrostatic charge boosting (ECB) technique for triboelectric energy harvesting to extract extra energy when C_T drops and avoid electrostatic energy loss when C_T rises. The rest of this paper will be divided into five sections: Section II introduces the mechanism of triboelectric energy harvesting and the proposed ECB strategy optimized for triboelectric energy harvesting strategy with theoretical analysis; Section III presents the proposed SC-ECB rectifier, highlighted in operation mechanism and performance analysis; Section IV presents the circuit implementation details of the proposed energy harvesting interface; Section V shows the measurement results; finally, Section VI draws the conclusion.

II. Proposed Technique and Analysis

A. Energy Transduction Mechanisms

In a TENG, one of the main energy transduction methods, which has been recognized by most prior works, is via the displacement of static surface charge on the triboelectric layer (Q_S). The value of Q_S is mainly determined by the parameters of TENG. The energy induced via this method has an alternating short-circuit current direction consistent with the direction of electrode movement and an open-circuit potential linear to the distance of movement, which shares similar features with the piezoelectric energy [8].

Nevertheless, Q_S is not the only one involved in electrostatic induction. The electrostatic charge on TENG electrodes (Q_T) also forms displacement current during movement and transduces energy. As the electrodes form a capacitor, the electrostatic energy generated by Q_T (E_{QT}) can be derived according to the formula of energy on a capacitor:

$$E_{QT} = \frac{1}{2}\frac{Q_T^2}{C_T} = \frac{1}{2}Q_T V_T \tag{1}$$

where E_{QT} is inversely proportional to C_T for a certain quantity of Q_T. Additionally, when C_T drops, higher Q_T contributes to more increases in electrostatic energy; on the contrary, when C_T rises, lower absolute amplitude of Q_T results in less electrostatic energy degradation, while in an extreme case, a zero-Q_T leads to zero electrostatic energy loss. Different from Q_S, Q_T, the key parameter in this energy transduction pathway, can be controlled by the back-end energy extractor. For example, when the SSHI technique is employed, the flipped V_T introduces initial Q_T on electrodes when C_T reaches the minimum or the maximum, which contributes to extra electrostatic energy harvested during decreasing-C_T semi-period but degrades electrostatic energy on C_T during increasing-C_T semi-period.

Therefore, the energy-extracting strategy purposed to maximize the overall energy output should be optimized considering the characteristics of electrostatic energy induced by Q_S and Q_T inclusively. As the energy induced by Q_S shares similar features with the piezoelectric energy harvesting, previous works employing the SSHI technique achieve good energy-extraction performance. However, optimization of harvesting electrostatic energy induced by Q_T has never been considered in previous works, and it actually contributes a significant part of the harvested energy.

B. Proposed ECB Technique

Hereby, an ECB technique for triboelectric energy harvesting is proposed, with the operation flow and waveforms

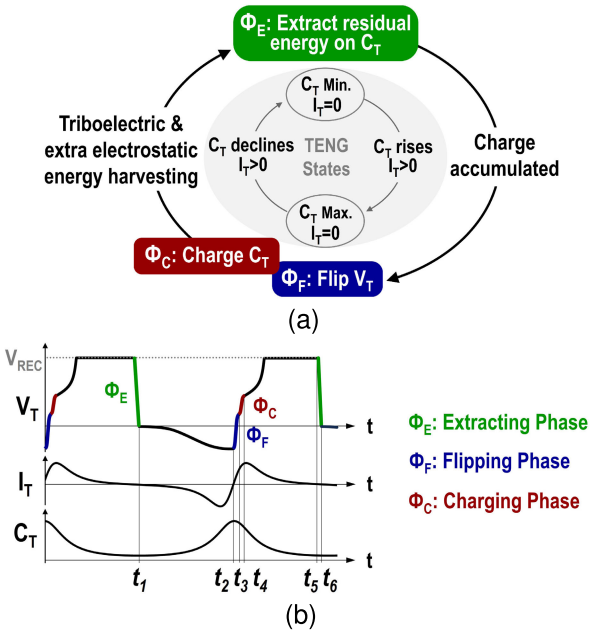

Fig. 3. (a) State machine and (b) waveforms of the proposed triboelectric energy harvesting strategy.

illustrated in Fig. 3 [27]. When C_T is at the minimum ($C_{T,\min}$) or I_T switches from positive to negative, the energy on C_T is extracted and temporarily stored on a storage capacitor. This phase is named the extracting phase (Φ_E). As V_T is equal to 0 V after the extraction, I_T will not be wasted in discharging C_T, and the degradation of electrostatic energy due to the impending increase in C_T in the next semi-period is minimized to the greatest extent. After half period, when C_T reaches the maximum ($C_{T,\max}$) or I_T switches from negative to positive, two sequential phases are introduced: the flipping phase (Φ_F) and the charging phase (Φ_C). During Φ_F, V_T is flipped to synchronize the direction of V_T and I_T and to increase Q_T. Then, during the following Φ_C phase, the charge extracted in Φ_E is dumped back to the TENG to charge up V_T. Since the energy extracted in Φ_E is at a high voltage level while that returned to TENG in Φ_C is at a low voltage level, the charge dumped back to TENG during Φ_C (Q_C) is theoretically possible to be larger than the charge extracted according to the law of energy conservation. Consequently, Q_T can be boosted in this process, and these extra charges returned to C_T when C_T is at the maximum will contribute to extra electrostatic energy harvested in the following decreasing-C_T semi-period, improving the overall triboelectric energy harvesting performance.

C. Performance Analysis

To verify the effectiveness of the proposed ECB technique, a comparative analysis is performed between the output power of the conventional SSHI technique and the proposed energy harvesting strategy. For simplicity, TENG is assumed to be operating under uniform sinusoidal vibration at a frequency of f_{op}. Additionally, the charge induced by Q_S in each semi-period (Q_{SC}) is assumed to be the same, which is identical to the amount of charge that I_T outputs in each semi-period and can be calculated by

$$Q_{SC} = \int_0^{\frac{T}{2}} I_T(t)dt = C_{T,\min} V_{\text{OC}} \tag{2}$$

where V_{OC} represents the open-circuit voltage amplitude of TENG.

When an SSHI rectifier is employed for energy harvesting, its power output can be derived in a similar procedure as [20, Eq. (30)], expressed below

$$\begin{aligned} \text{P}_{\text{SSHI}} = &(\eta_{F,\text{P}}\eta_{F,\text{N}} - 1) f_{\text{op}} C_{T,\min} V_{\text{REC}}^2 \\ &+ (\eta_{F,\text{N}} + 1) f_{\text{op}} C_{T,\min} V_{\text{OC}} V_{\text{REC}} \end{aligned} \tag{3}$$

where $\eta_{F,\text{P}}$ and $\eta_{F,\text{N}}$ are the flipping efficiency when V_T is flipped with the directions of positive-to-negative and negative-to-positive, respectively; β is the varying ratio of C_T given by $\beta = C_{T,\max}/C_{T,\min}$. The diode forward voltage is neglected. This expression is effective under the condition $V_{\text{REC}} > V_{\text{OC}}/(\beta - 1)$, which corresponds to the physical situation that V_T will not reach $-V_{\text{REC}}$ during the negative-V_T semi-period due to the relatively high V_{REC} or large β [20]. In this case, due to the flipping loss, $\eta_{F,\text{P}}$ and $\eta_{F,\text{N}}$ are always lower than 100%; thus, the power output of SSHI rectifier mathematically performs as a parabola opening downward with respect to V_{REC}.

Regarding the proposed ECB technique, the general expression of the output power can be written as

$$\text{P}_{\text{ECB}} = f_{\text{op}} Q_{\text{HAV}} V_{\text{REC}} \tag{4}$$

where Q_{HAV} represents the charge transferred to the output capacitor in one period, assuming that V_T does not reach $-V_{\text{REC}}$ during the negative-V_T semi-period. Thanks to the lower V_T in this semi-period due to the ECB strategy, the requirement to V_{REC} now becomes to $V_{\text{REC}} > V_{\text{OC}}/\beta$. To calculate Q_{HAV} in one period from t_1 to t_6 in Fig. 3(b), we need to calculate the charge accumulated in the TENG in this period, which can be expressed below

$$Q_{\text{HAV}} = \eta_F Q_{SC} + Q_C + Q_{SC} - C_{T,\min} V_{\text{REC}}. \tag{5}$$

Starting from t_1, C_T is completely out of charge. The first term $\eta_F Q_{SC}$ is the amount of charge stored in C_T at t_3, representing the flipped charge from the total charge generated in the negative-I_T semi-period; the second term Q_C is the charge dumped to C_T during the Φ_C phase between t_3 and t_4; the third term Q_{SC} is the TENG-generated charge in the positive-I_T semi-period; the last term $C_{T,\min} V_{\text{REC}}$ is the lost charge of C_T due to the extracting phase Φ_E. As Q_C originates from the charge extracted during Φ_E, we note the charge-boosting coefficient, α, as the ratio of the charge returned to C_T in Φ_C, over the charge extracted from C_T in Φ_E. It can be expressed as

$$\alpha = \frac{Q_C}{C_{T,\min} V_{\text{REC}}}. \tag{6}$$

Combining (2)–(6), the output power of the proposed ECB strategy given in (4) can be rewritten as

$$\begin{aligned} \text{P}_{\text{ECB}} = &(\alpha - 1) f_{\text{op}} C_{T,\min} V_{\text{REC}}^2 \\ &+ (\eta_F + 1) f_{\text{op}} C_{T,\min} V_{\text{OC}} V_{\text{REC}}. \end{aligned} \tag{7}$$

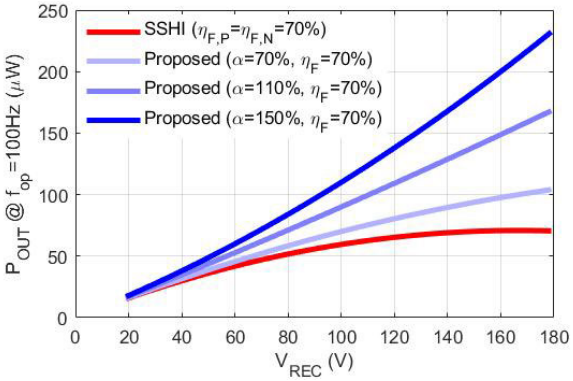

Fig. 4. Theoretical power output with respect to rectification voltage at different flipping efficiency (η_F) and charge transfer efficiency (α) under the conditions of $\beta = 10$, $f_{\rm op} = 100$ Hz, $C_{T,\rm min} = 50$ pF, $V_{\rm OC} = 100$ V.

It is clear that the polarity of the quadratic term in (7) is determined by whether α is larger or smaller than 100%. Fig. 4 illustrates the waveforms of the output power with respect to $V_{\rm REC}$ of the SSHI technique and the proposed energy harvesting strategy with different α. A greater α, namely a larger amount of Q_C, contributes to the harvesting of more electrostatic energy and, consequently, better performance than the SSHI rectifier. As aforementioned, Q_C can be boosted higher than $C_{T,\rm min}V_{\rm REC}$, i.e., $\alpha > 100\%$; thus, the coefficient of the quadratic term in (7) becomes positive, which means the power output of the proposed topology increases quadratically with respect to $V_{\rm REC}$. In this case, the maximum power point (MPP) will always be located at the maximum $V_{\rm REC}$, which is usually the breakdown voltage of the circuit. As a result, tracking the MPP of the proposed extractor becomes simple to implement.

Under the proposed ECB strategy, α has a ceiling value when the energy conversion from Φ_E to Φ_C is lossless, which can be derived as

$$\alpha_{\max} = \sqrt{\beta + \left(\eta_F \frac{V_{\rm OC}}{V_{\rm REC}}\right)^2} - \eta_F \frac{V_{\rm OC}}{V_{\rm REC}}. \tag{8}$$

In the case of $\alpha = \alpha_{\max}$, after substituting (8) into $\alpha_{\max} > 1$, the requirement for TENG to achieve possible $\alpha > 1$ could be derived as

$$\beta > 1 + 2\eta_F \frac{V_{\rm OC}}{V_{\rm REC}}. \tag{9}$$

From experiment validations, it is found that this relation can be easily satisfied for contact-separation TENGs. Therefore, in most triboelectric energy harvesting cases, employing the ECB technique can achieve charge and output power boosting, and consequently better output performance than the SSHI technique.

III. Proposed Rectifier With ECB Technique

A. Operation Mechanism

Hereby, we propose a SC-ECB rectifier to realize the aforementioned optimum triboelectric energy harvesting strategy. The architecture of the proposed rectifier is presented in Fig. 5. The synchronized charge boosting (SCB) block reconfigures three on-chip capacitors $C_{B1\sim3}$ to realize the extracting and charging operations and boost the charge from Φ_E phase to Φ_C phase to achieve $\alpha > 100\%$. The capacitor-based flipping (CBF) block contains four on-chip capacitors $C_{F1\sim4}$ to flip V_T voltage during the Φ_F phase. When either of these two blocks is activated, the active FBR (A-FBR) block grounds either side of TENG to build the current loop for the operations; additionally, it rectifies the ac energy from TENG.

The sequential configuration of capacitors, the waveform of V_T, and switch phases are shown in Fig. 6. When I_T in TENG crosses zero and C_T is at the minimum, Φ_E phase starts, with the SCB block involved. $C_{B1\sim3}$ are first placed in series and connected to C_T. The series configuration maximizes the voltage on the SCB block and thus minimizes the charge-sharing loss. From the perspective of charge conversion, the total charge stored in $C_{B1\sim3}$ is triple times of the charge flowing out from C_T. Then, to extract as much charge as possible, a phase-splitting technique is employed in the following extended subphases (2∼6) as presented in Fig. 6(a) [26]. The subphases are selected with decreasing voltage to ensure that the charge is dumped from C_T to the SCB block as much as possible. Besides, the sequence of $C_{B1\sim3}$ is designed based on the different voltage tolerance of capacitors. In this way, C_{B3} holds the highest voltage, while C_{B1} holds the second highest and C_{B2} tolerates the lowest. At the end of the Φ_E phase, the remaining charge on C_T is cleared to avoid discharging loss due to the negative-I_T. When I_T crosses zero again but with C_T at the maximum, phase Φ_F and Φ_C are engaged in turn. The flipping capacitor array in the BF block flips the charge in C_T sequentially, employing the parallel-SSHC configuration [shown in Fig. 6(b)] [25]. After the flipping, the three capacitors in the SCB block dump charge to C_T in a sequence from low voltage to high voltage [shown in Fig. 6(c)]. In this way, the extra charge gained in the Φ_E is expected to be returned to C_T to achieve $Q_C > C_{T,\rm min}V_{\rm REC}$, i.e., $\alpha > 100\%$.

B. Performance Analysis of the Proposed Rectifier

In this section, the theoretical performance of the proposed SC-ECB rectifier is analyzed mathematically. The capacitors in the SCB stage are designed to have the same capacitance C_B, i.e., $C_{B1} = C_{B2} = C_{B3} = C_B$. The mathematical expression of the charge-boosting coefficient of the proposed rectifier, $\alpha_{\rm ECB}$, is complex due to the phase-splitting operation. Fortunately, its expression when excluding the extended extraction subphases can be simply derived as follows:

$$\alpha_{\rm ECB} = \frac{1}{1/3 + C_{T,\rm min}/C_B + 2/\beta}\left(1 - \frac{\eta_F}{\beta}\frac{V_{\rm OC}}{V_{\rm REC}}\right). \tag{10}$$

It can be observed that a larger $\alpha_{\rm ECB}$ benefits from large C_B, high $V_{\rm REC}$, and large β (varying ratio of C_T). Additionally, this expression helps determine the conditions for achieving $\alpha_{\rm ECB} > 100\%$. Among all parameters in this equation, C_B and $V_{\rm REC}$ are the parameters that can be controlled by the energy harvesting interface. To minimize chip area usage, C_B is designed to be equal to $C_{T,\max}$ (or $\beta C_{T,\rm min}$). After setting

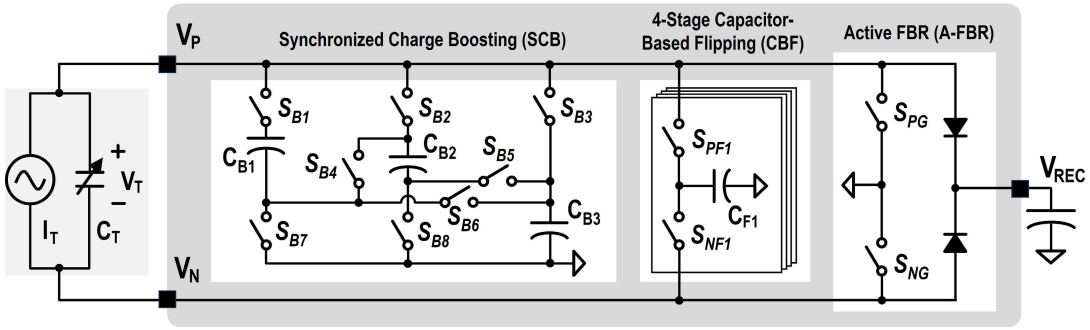

Fig. 5. Topology of the proposed SC-ECB rectifier.

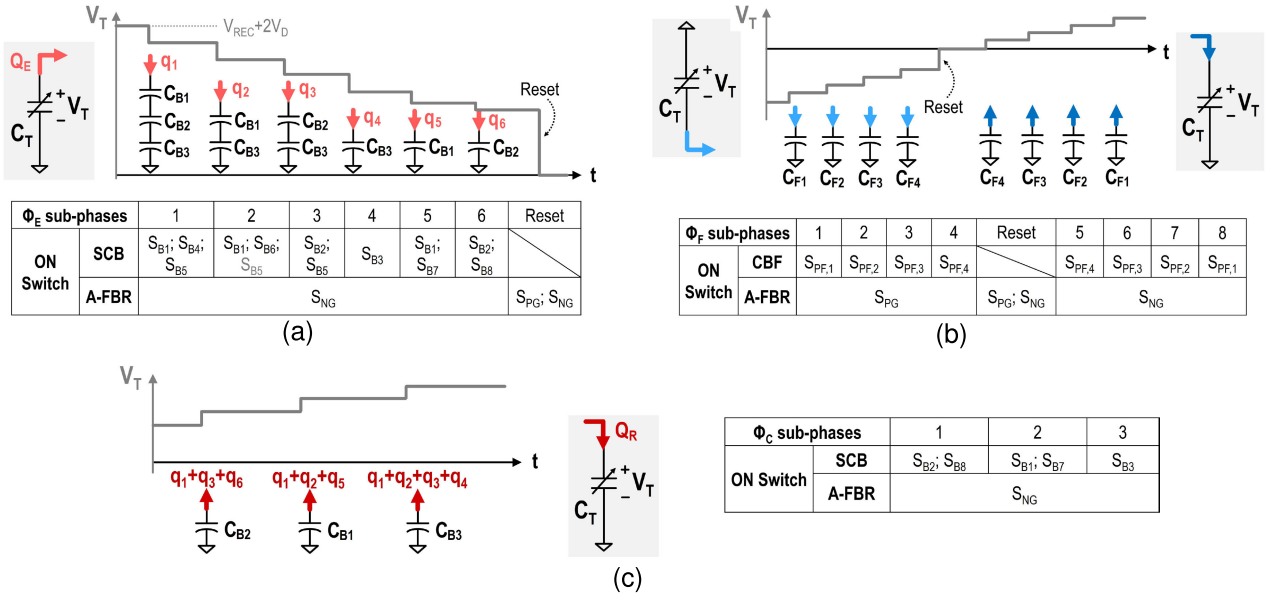

Φ_E sub-phases		1	2	3	4	5	6	Reset
ON Switch	SCB	S_{B1}; S_{B4}; S_{B5}	S_{B1}; S_{B6}; S_{B5}	S_{B2}; S_{B5}	S_{B3}	S_{B1}; S_{B7}	S_{B2}; S_{B8}	
	A-FBR	S_{NG}						S_{PG}; S_{NG}

Φ_F sub-phases		1	2	3	4	Reset	5	6	7	8
ON Switch	CBF	$S_{PF,1}$	$S_{PF,2}$	$S_{PF,3}$	$S_{PF,4}$		$S_{PF,4}$	$S_{PF,3}$	$S_{PF,2}$	$S_{PF,1}$
	A-FBR	S_{PG}				S_{PG}; S_{NG}	S_{NG}			

Φ_C sub-phases		1	2	3
ON Switch	SCB	S_{B2}; S_{B8}	S_{B1}; S_{B7}	S_{B3}
	A-FBR	S_{NG}		

Fig. 6. Configuration of capacitors, waveform of V_T, and the power switches turned on in (a) extracting phase Φ_E, (b) flipping phase Φ_F, and (c) charging phase Φ_C.

$\alpha_{\text{ECB}} > 100\%$, the following relationship is obtained:

$$\frac{1}{\beta}\left(3+\eta_F\frac{V_{\text{OC}}}{V_{\text{REC}}}\right)<\frac{2}{3} \tag{11}$$

$$\Rightarrow V_{\text{REC}}>\frac{3}{2\beta-9}\eta_F V_{\text{OC}}. \tag{12}$$

Next, the contribution of the extended extracting subphases is evaluated. In some of these subphases, two capacitors are connected in series, where the charge is doubled when transferred from C_T to $C_{B1\sim3}$; thus, the extra charge dumped to C_T contributed by the extended subphases is derived as

$$Q_{\text{extra}}=2q_2+2q_3+q_4+q_5+q_6. \tag{13}$$

However, the extra charge also increases the voltage across both C_T and $C_{B1\sim3}$, resulting in less charge extracted in the first subphase. The reduced part can be derived as

$$Q_{\text{loss}}=\frac{9}{\beta+3}\left(q_2+\frac{4}{3}q_3+\frac{1}{3}q_4+\frac{2}{3}q_5+q_6\right). \tag{14}$$

Setting $Q_{\text{extra}} > Q_{\text{loss}}$, it can be found that when $\beta > 6$, Q_{extra} is always larger than Q_{loss}. Consequently, the phase-splitting technique can positively contribute to the charge boosting, leading to quadratically increasing power output according to our analysis in Section II-B. Fortunately, $\beta > 6$ is possible to be achieved in most TENGs, including the TENG used in this work. Therefore, the proposed SC-ECB can realize $\alpha_{\text{ECB}} > 100\%$ and consequently, a quadratically increasing output power regarding V_{REC}.

IV. Circuit Implementations

A. System Architecture

The architecture of the proposed system is presented in Fig. 7. The chip consists of two major regions: a high-voltage (HV) region and a low-voltage (LV) region, which are interfaced by switch drivers. The HV region consists of the proposed rectifier and a dc–dc buck converter for maximum power point tracking (MPPT). Each device in the HV region must gain enough voltage tolerance. The HV switches are implemented with laterally diffused MOSs (LDMOSs), which have a breakdown voltage of up to 70 V. Each HV switch is adapted to the voltage range across it when cutting off and driven by specific switch drivers. Besides, the implementation of on-chip capacitors is considered as well. To effectively boost charge, each of $C_{B1\sim3}$ is set as 180 pF. The metal-insulator-metal capacitor (MIMCap) is advantageous in high

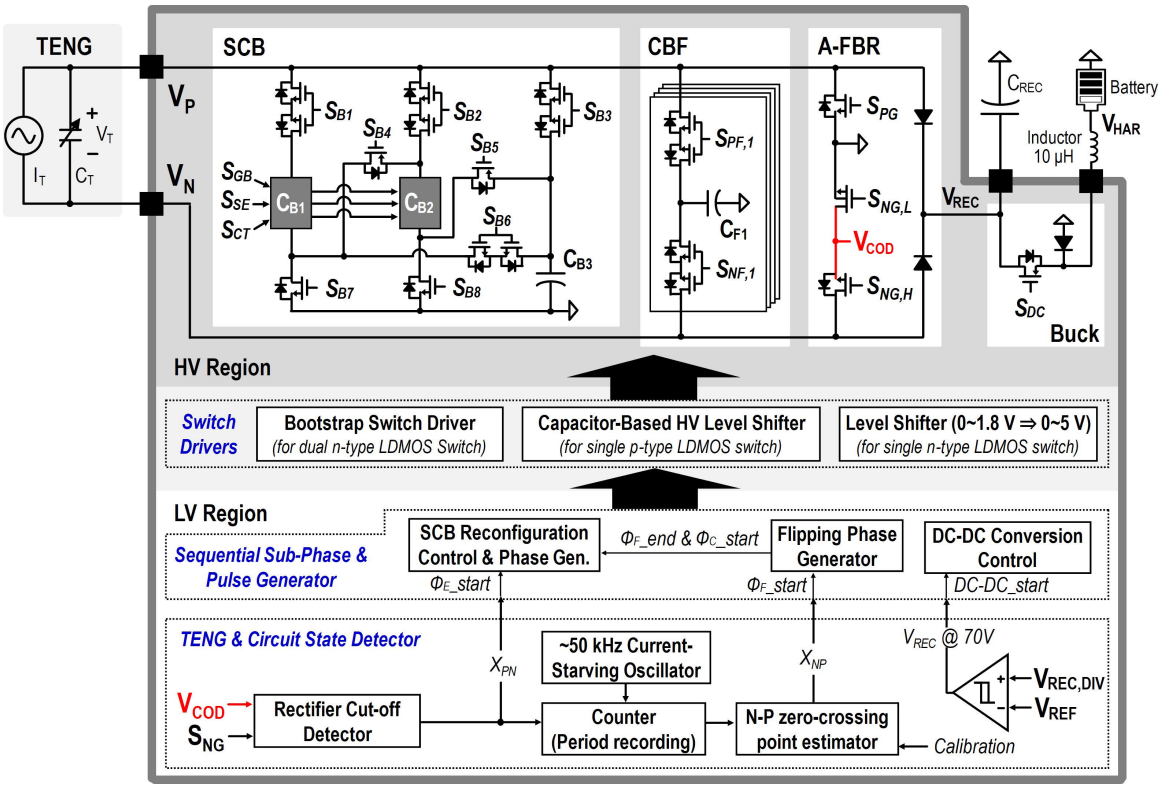

Fig. 7. Top-level architecture of the proposed triboelectric energy harvesting system.

capacitance density and little parasitics. Nonetheless, its technical voltage is 5 V only, much lower than that needed for ECB. Therefore, C_{B1} and C_{B2} in the SCB block stacks three and two MIMCaps to achieve 15 and 10 V voltage tolerance, respectively, which occupies a large area of the top metals. To save the chip area, C_{B3} and the flipping capacitors in the CBF block are implemented with metal-oxide-metal capacitors (MOMCaps), which can tolerate 70 V intrinsically. To minimize the top- and bottom-plate losses of MOMCaps, C_{B3} and the flipping capacitors have one node always grounded. Finally, to regulate V_{REC} for the MPPT purpose, an asynchronous dc–dc buck converter operating at discontinuous conduction mode (DCM) is employed with a small off-chip inductor (10 μH) for miniaturization. Due to the high input voltage and the small inductor, S_{DC} is turned on for a short period (around 40 ns) to minimize the conduction loss.

The LV region contains associated sensing and control blocks operating at 1.8 V. The positive-to-negative I_T switching moment (X_{PN}), which is also the starting trigger of the phase Φ_E, is sensed by the rectifier cutoff detector. The combination of a digital counter and a current-starving oscillator operating at around 50 kHz is implemented to sample and digitize the time interval between the two consecutive positive-to-negative I_T switching moments, which is the measured operating period of the TENG. Then, the digital N-P zero-crossing point estimator processes the operation period and predicts the negative-to-positive zero-crossing moment of I_T (X_{NP}), which should come half-period after the positive-to-negative I_T switching moment. The signals X_{PN} and X_{NP} are sent to logical blocks to generate switch driving signals in Φ_E, Φ_F, and Φ_C phases. In the LV region, a breakdown protection block is employed, which is composed of a dc–dc conversion control and a V_{REC} monitor. A hysteresis comparator is employed to sense the divided rectification voltage. The dc–dc conversion control block generates the short pulses for S_{DC} and adjusts the pulse quantity based on the extracted power. Thanks to the proposed ECB technique, the breakdown protection also performs MPPT by regulating V_{REC} at the breakdown voltage to keep the system at the MPP.

B. HV Switches and Drivers

To adapt different voltage ranges and optimize the area, three types of HV switches are implemented. The dual n-type LDMOS switch contains two n-type LDMOS, with their source terminals connected. This structure prevents latch-up through the body diode and thus can be utilized to isolate any voltage nodes. To drive this switch, a bootstrap gate driver is implemented, with the circuit diagram presented in Fig. 8. Protection circuit indicated by the gray regions is employed to protect the cross-coupled 5-V PMOSs. This bootstrap gate driver is advantageous in low static power consumption. The single p-type LDMOS switch is used if the voltage at its source terminal is higher than that at the drain terminal when it is intended to open. It is driven by the capacitor-based HV level shifter as shown in Fig. 9, which has no static power consumption except leakage. The MOMCaps are used to isolate the HV region and the LV control and buffers. Considering extra parasitics from the LDMOS, the MOMCap connected to the gate of the p-type LDMOS is larger than the

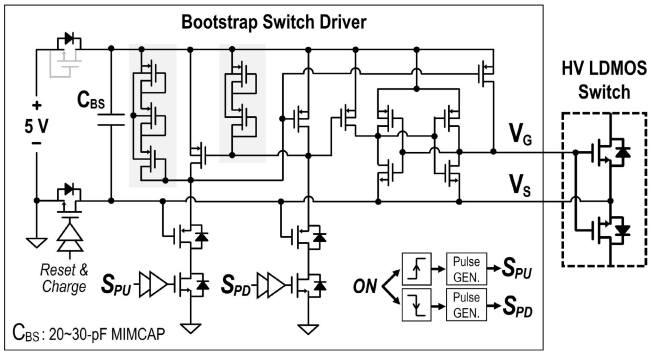

Fig. 8. Circuit diagram of the bootstrap gate driver.

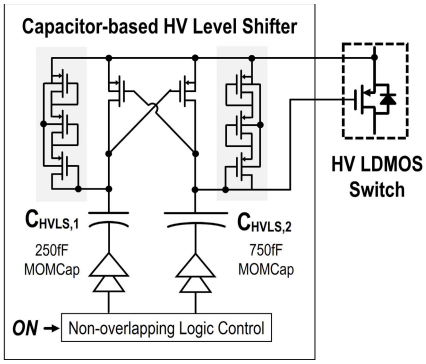

Fig. 9. Circuit diagram of the capacitor-based HV level shifter.

other one. The last type of HV switch is the single n-type LDMOS switch employed when isolating one node from the ground, which is driven by a typical level shifter and buffer stages customized according to the size of the n-type LDMOS.

C. Stacking-MIM Capacitors and SCB Reconfiguration Control

The implementation details and operation mechanism of the stacked capacitors are presented in Fig. 10. The stacked capacitors are configured in series in Φ_E and Φ_C, with the direction of the body diodes of S_{SE} consistent with the current flow in the phase Φ_E but reverse to that in the phase Φ_C. As the voltage across the MIMCaps drops during Φ_C, the capacitor-based HV level shifters that drive S_{SE} are switched on and off twice to maintain a negative gate-source voltage and settle the charge sharing. Due to the parasitic and mismatch on capacitance, the voltage across each MIMCap after the series configuration could differ. To maximize the voltage tolerance, the charge among the stacked MIMCaps is balanced with parallel configurations after Φ_C. During the balancing phase, the bottom plates of MIMCaps are grounded via S_{GB} while their top plates are connected via S_{CT}. Due to the varying voltage level on the top plate of MIMCaps, S_{CT} employ dual n-type LDMOS switches and are driven by bootstrap gate drivers.

Fig. 11 shows the architecture of the SCB reconfiguration control and phase generator block and the illustrated waveform of the key signals and V_T. A ring oscillator is used to generate a clock signal, which is only powered on during Φ_E and Φ_C. The clock frequency is divided by D-flip-flop to generate sequential subphases in Φ_E and Φ_C, respectively. In each subphase, the power switches are turned on at the rising edge of the synchronized signal OFF2ON and turned off at the rising edge of the signal ON2OFF to ensure nonoverlapping between configurations. Due to the different number of triggers of series configuration in Φ_E and Φ_C, the subphase period also differs.

D. Rectifier COD

In previous works, the zero-crossing moment is found by detecting the voltage drop at the high voltage side of V_{P} or V_{N}. To protect the LV comparator, a capacitor ladder [21] or an OFF-state LDMOS [19] is utilized to isolate the high-level dc voltage and bypass the voltage drop, which leads to extra charging and parasitic loss or suffers from low sensitivity. In this work, a novel rectifier cutoff detection (COD) method is proposed, which is part of the A-FBR and tracks the positive-to-negative I_T switching moment by detecting the moment when A-FBR switches states at the low voltage side, i.e., V_{N}. The topology and the operational waveform are shown in Fig. 12. When sensing the positive-to-negative I_T switching moment, $S_{NG,L}$ in A-FBR is turned off to use its body diode, and $S_{NG,H}$ is marginally turned on to follow V_{N} until 1.8 V, to keep the V_{COD} in a safe input range of the comparator [28]. When I_T is positive, V_{COD} is equal to $-V_{\mathrm{TH}}$ due to the forward voltage drop. Then, when I_T switches to a negative direction, V_T will start to drop while, meanwhile, V_{N} is going to rise. When V_{COD} crosses 0 V, the comparator is triggered, and a COD signal is generated to start the phase Φ_E. In this way, only an extra 5 V MOSFET is used, which introduces little parasitics and takes small area. Besides, this method is practical in any case regardless of the rectification voltage.

V. Measurement Results

The proposed triboelectric energy harvesting interface was fabricated in a 180-nm BCD process, with an active area of 3.2 mm^2, shown in Fig. 13. Fig. 14 shows the experimental setup and the in-house fabricated contact-separation TENG driven by a shaker. The TENG utilizes Kapton as the triboelectric layer and has a contact area of 3600 mm^2 (60 $\times$ 60 mm). During experiments, a 150-Hz vibration is applied on one plate via a shaker. According to the measurements, this TENG has a minimum capacitance of approximately $C_{T,\min} = 30$ pF and a maximum capacitance of approximately $C_{T,\max} = 230$ pF. Hence, the capacitance varying ratio β is around 7.7, meeting the requirement of $\beta > 6$ for achieving quadratically increasing power output from the proposed rectifier. Its open-circuit voltage is measured to be around 100 V. Regarding the off-chip components, an 1 μF capacitor is employed as C_{REC} to measure the output power, and a 10 μH inductor is employed for the buck converter.

The measured waveforms of the V_{REC}, V_{P}, V_{N}, and the clock signal (C_CLK) during the three major phases are shown in Fig. 15. The left-top subfigure shows the waveform when the rectifier extracts energy under several kinetic periods of the TENG. The waveform during the Φ_E phase is zoomed in and presented at the top-right. It can be observed that

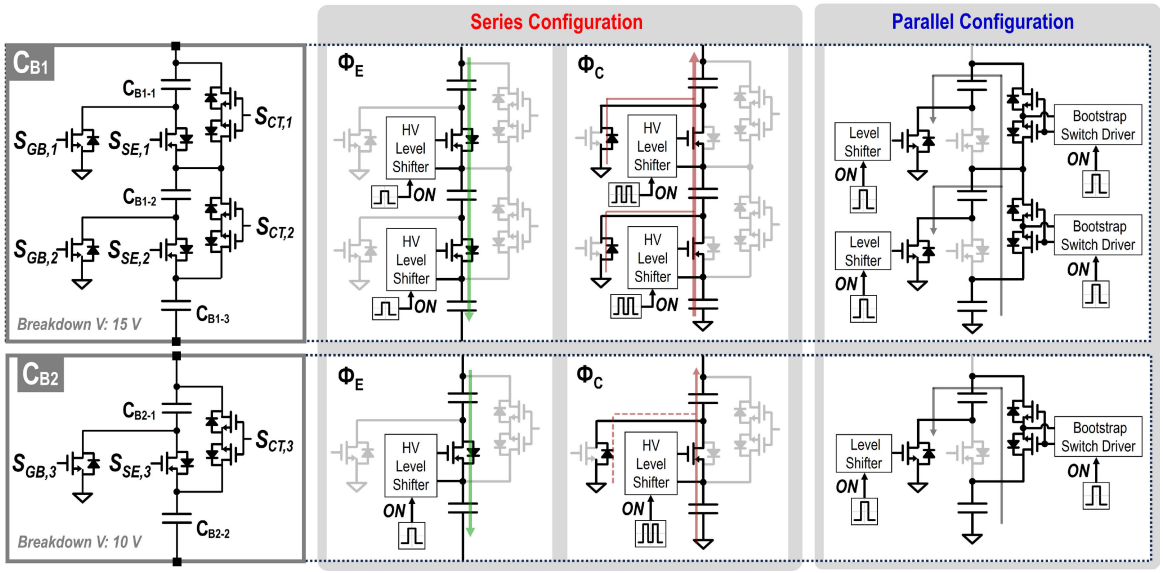

Fig. 10. Circuit diagram and operations of the stacking-MIM capacitors.

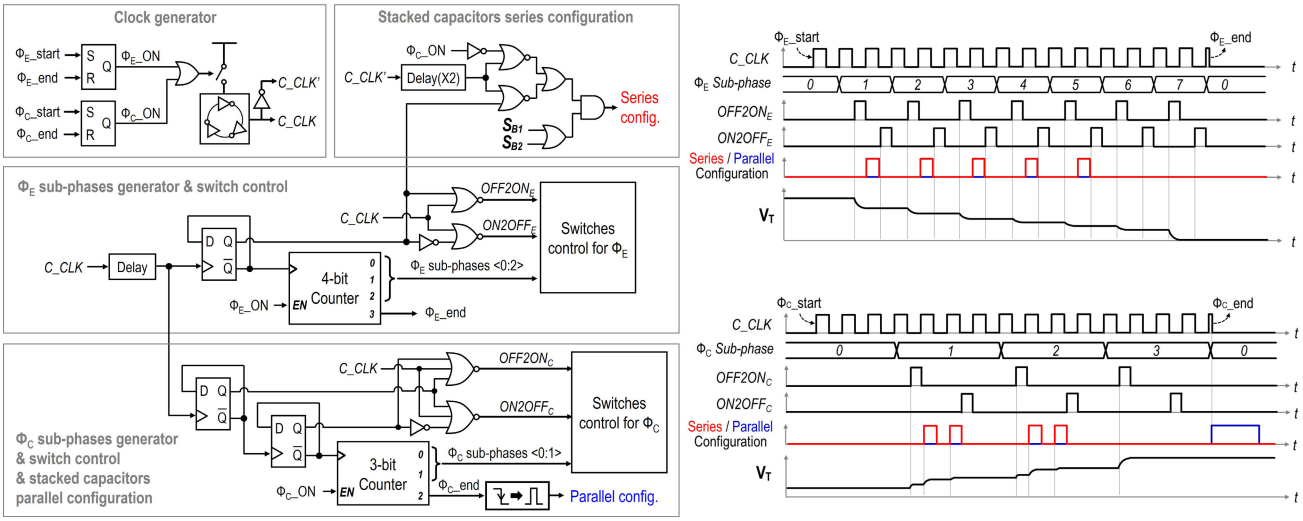

Fig. 11. Circuit diagram and operation waveform of the ECB reconfiguration control and phase generator.

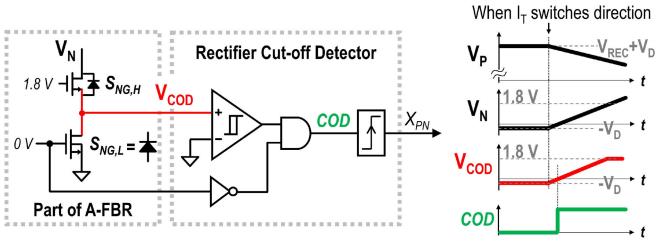

Fig. 12. Circuit diagram and the operational waveform of the rectifier COD.

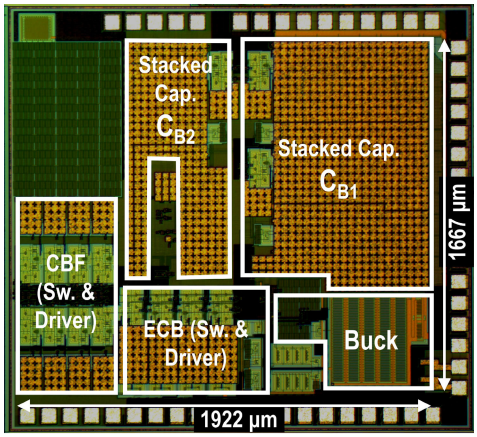

Fig. 13. Chip micrograph.

the charge on the TENG is extracted by the ECB block in six subphases. Overall, it takes 16 C_CLK cycles to finish the energy extraction to guarantee sufficient charge transfer time for each subphase and nonoverlapping time between adjacent subphases. The waveform during Φ_F and Φ_C phases is presented at the bottom of Fig. 15. Φ_F performs V_T voltage flipping, and it is implemented in nine subphases with four flying capacitors, similar to that in a parallel-SSHC rectifier. The Φ_C phase follows, and it consists of three subphases. The charge dumping can be observed to be synchronized with

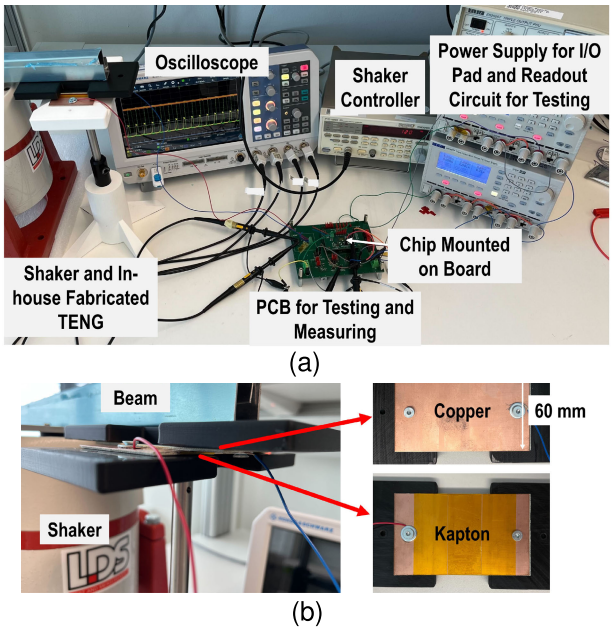

Fig. 14. (a) Experimental setup and (b) in-house fabricated contact-separation TENG driven by a shaker.

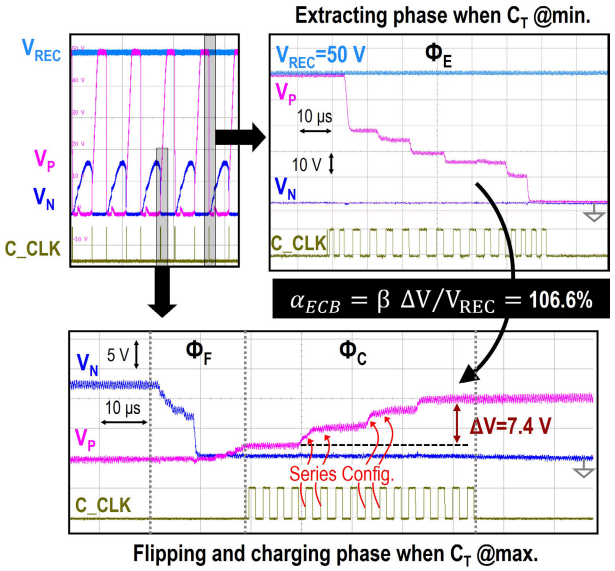

Fig. 15. Measured transient waveform showing the operation of the proposed rectifier.

the rising edge of the signal C_CLK, consistent with the operations presented in Fig. 11. The voltage rise during Φ_C is measured 7.4 V when V_{REC} is equal to 50 V. By substituting the values into (6), the charge-boosting coefficient α can be calculated as 106.6%, which demonstrates the effectiveness of the proposed SC-ECB rectifier that achieves charge boosting.

Fig. 16 shows the measured operation of the COD block when V_{REC} is around 70 V. The extraction operation is triggered by the rising edge of the signal COD, i.e., the detected zero-crossing point. The voltage drop at this moment is 1.5 V, which is only around 2.1% of V_{REC}. The detection delay of the low-power (around 20 nW) hysteresis comparator shown at the bottom is 153 μs, which is negligible compared to the operating frequency of the TENG.

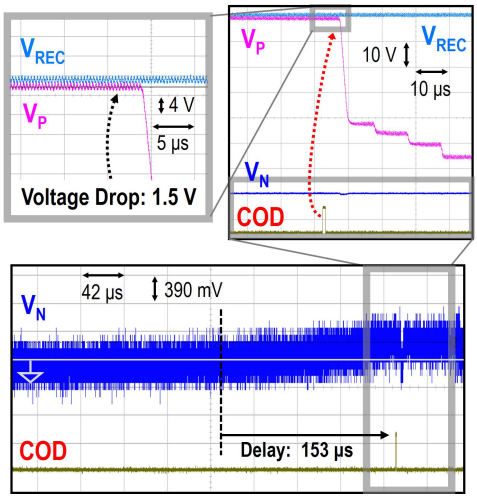

Fig. 16. Measured transient waveform showing the operation of the rectifier COD.

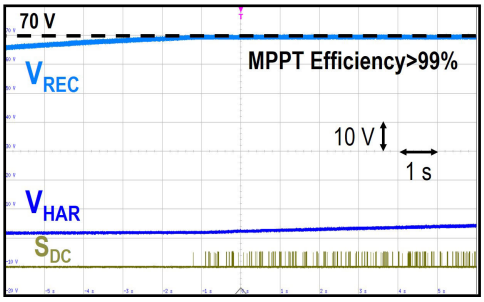

Fig. 17. Measured transient waveform showing when the system is entering the MPP and when it is operating at MPP.

Fig. 17 shows the measured operation waveform when the system is entering the MPP and continues operating at the MPP. Since the BCD process has a breakdown voltage of 70 V, when V_{REC} reaches 70 V, a dc–dc buck converter is turned on to transfer an amount of energy from C_{REC} to C_{HAR} to lower V_{REC}. The signal S_{DS} is the switching signal of the buck converter. It can observed that after S_{DS} becomes active, V_{REC} keeps around 70 V and V_{HAR} starts increasing. The pulsewidth of S_{DC} is designed to be short to maintain a small V_{REC} ripple of less than 1 V. Thanks to the proposed ECB technique, the MPP of the proposed rectifier is also located at 70 V; thus, the good V_{REC} regulation performance also results in an MPPT efficiency of around 99% in steady states. If the proposed system is integrated with devices with higher breakdown voltages, or with chip-stacking techniques [21], the output power is likely to go significantly higher due to the quadratic power curve.

The measured output power of the proposed rectifier is shown in Fig. 18. A quadratically increasing P_{EXT} can be observed when V_{REC} is between 25 and 50 V, which is consistent with the measured α_{ECB} within this range where it is higher than 100% as shown in Fig. 19. This demonstrates the correctness of the theoretical analysis. However, the increase of P_{EXT} slows down when V_{REC} is higher than 50 V. This is mainly due to the increased leakage and parasitic loss of the capacitors in the SCB block. This leads to the degradation of α_{ECB} which drops lower than 100% for high V_{REC}. Within

TABLE I
COMPARISON TABLE OF THE STATE-OF-THE-ARTS

	ISSCC'15 [29]	JSSC'20 [12]	JSSC'21 [13]	TCAS-I'21 [19]	JSSC'22 [21]		**This work**
Process	0.25-μm BCD	0.18-μm BCD	0.18-μm BCD	0.18-μm BCD	0.18-μm BCD		**0.18-μm BCD**
Transducer	Electret Gen.	CS-TENG	CS-TENG	CS-TENG	Wind-TENG		**CS-TENG**
Op. Frequency (Hz)	N/A	50 - 60	40 - 50	1 - 5	250		**150**
Inherent Capacitance	Varying	Varying	Varying	Varying	Constant		**Varying**
Energy Harvesting	Electrostatic	Triboelectric	Triboelectric	Triboelectric	Triboelectric		**Triboelectric**
Energy Extraction Methods	FBR	Dual-Output FBR	Dual-Output FBR	P-SSHI	Scalable MCS-BF		**ECB**
Bias-flip	N/A	N/A	N/A	Inductor-based	Inductor-based		**Capacitor-based**
Fully Integrated at Rectifier Stage	Yes	Yes	Yes	No	No		**Yes**
Max. Input Voltage (V)	60	70	70	70	130 (2-chip)	195 (3-chip)	**70**
MPPT Method	P&O	FOCV	FOCV	N/A	N/A	N/A	**Auto-MPPT @Breakdown Voltage**
MPPT Efficiency (%)	99	97	89.7	N/A	N/A	N/A	**99**
External Inductor	10 mH	1 mH	10 mH	1 mH	10 mH		**10 μH (For DC-DC only)**
Extracted Power (μW)	1-1000	4.5 – 16	3.9 – 10.5	722	1211	823	**127.6**
P_{EXT}/P_{FBR}	N/A	N/A	N/A	1.62×	3.14×	2.14×	**14.0×**

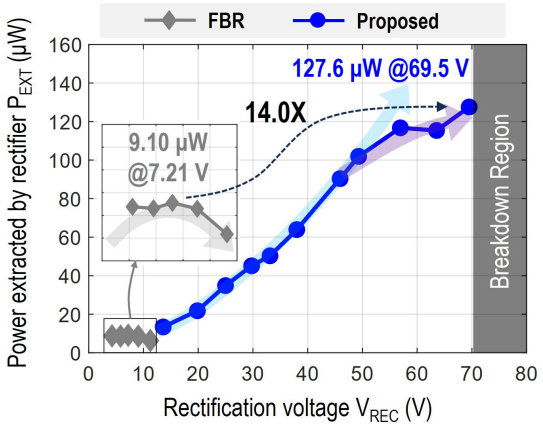

Fig. 18. Measured performance showing P_{EXT} versus V_{REC}.

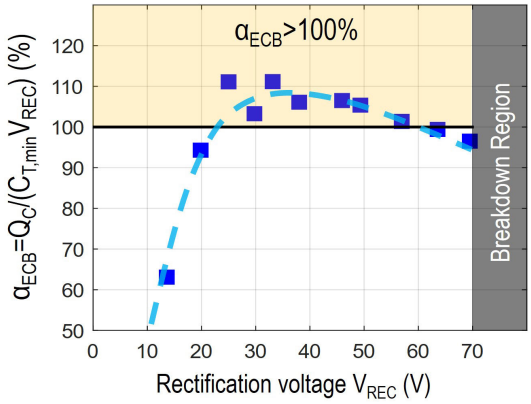

Fig. 19. Measured performance showing α_{ECB} versus V_{REC}.

the 70-V breakdown voltage domain, the proposed SC-ECB rectifier extracts 127.6 μW peak power when V_{REC} is 69.5 V, which is 14 times higher than the power output using a passive FBR.

Table I compares this work with the state-of-the-art designs. Similar to a conventional electrostatic energy harvester, a TENG also has a varying capacitance, but it is advantageous in self-sustained excitation without the requirement of external energy sources. In prior triboelectric energy harvesting interface designs, extracting the potential electrostatic energy due to the varying C_T has not been studied or designed. With the ECB technique, the proposed rectifier can utilize the self-excited electrical energy from TENG to extract extra electrostatic energy. As a result, it achieves an MPPT efficiency of 99% with constant MPP at the breakdown voltage of the circuit and the highest power extraction enhancement among the listed works. Besides, thanks to the capacitor-based BF and ECB techniques, this work is the first fully integrated active rectifier for triboelectric energy harvesting. For the dc–dc conversion stage following the rectifier, a 10 μH inductor is employed, which has a much smaller form factor compared to the inductors used in previous works.

VI. CONCLUSION

This article presents a fully integrated BF rectifier with a capacitor-based ECB technique for triboelectric energy harvesting. The proposed rectifier addresses the electrostatic energy degradation that occurs due to the varying intrinsic

capacitance of a TENG and boosts the electrostatic energy harvesting by synchronously dumping charge on TENG. Consequently, a quadratically increasing output power of TENG regarding rectification voltage is obtained, achieving a constant MPP at the breakdown voltage of the circuit. Additionally, since the rectifier stage employs no inductor, it can be fully integrated on-chip for miniaturization and low leakage. A 14-fold improvement in the energy extraction performance compared to the FBR is achieved.

ACKNOWLEDGMENT

The authors would like to thank Lukasz Pakula for his help in TENG fabrication and Zu Yao Chang for his help in wire bonding and PCB design.

REFERENCES

[1] L. Zhou, D. Liu, J. Wang, and Z. L. Wang, "Triboelectric nanogenerators: Fundamental physics and potential applications," *Friction*, vol. 8, no. 3, pp. 481–506, Jun. 2020.

[2] J. S. Y. Tan et al., "A fully energy-autonomous temperature-to-time converter powered by a triboelectric energy harvester for biomedical applications," *IEEE J. Solid-State Circuits*, vol. 56, no. 10, pp. 2913–2923, Oct. 2021.

[3] H. Ouyang et al., "Symbiotic cardiac pacemaker," *Nature Commun.*, vol. 10, no. 1, p. 1821, Apr. 2019.

[4] B. Huang, P. Wang, L. Wang, S. Yang, and D. Wu, "Recent advances in ocean wave energy harvesting by triboelectric nanogenerator: An overview," *Nanotechnol. Rev.*, vol. 9, no. 1, pp. 716–735, Aug. 2020.

[5] Z. Ren, L. Wu, Y. Pang, W. Zhang, and R. Yang, "Strategies for effectively harvesting wind energy based on triboelectric nanogenerators," *Nano Energy*, vol. 100, Sep. 2022, Art. no. 107522.

[6] R. Hinchet et al., "Transcutaneous ultrasound energy harvesting using capacitive triboelectric technology," *Science*, vol. 365, no. 6452, pp. 491–494, Aug. 2019.

[7] X. Liu et al., "An ultrasound-driven implantable wireless energy harvesting system using a triboelectric transducer," *Matter*, vol. 5, no. 12, pp. 4315–4331, Dec. 2022.

[8] W. Peng and S. Du, "The advances in conversion techniques in triboelectric energy harvesting: A review," *IEEE Trans. Circuits Syst. I, Reg. Papers*, vol. 70, no. 7, pp. 3049–3062, Jul. 2023, doi: 10.1109/TCSI.2023.3261780.

[9] K. Rawy, R. Sharma, H.-J. Yoon, U. Khan, S.-W. Kim, and T. T.-H. Kim, "A triboelectric nanogenerator energy harvesting system based on load-aware control for input power from 2.4 μW to 15.6 μW," *Nano Energy*, vol. 74, Aug. 2020, Art. no. 104839.

[10] S. C. Chandrarathna, S. A. Graham, M. Ali, J. S. Yu, and J. Lee, "An efficient power management system using dynamically configured multiple triboelectric nanogenerators and dual-parameter maximum power point tracking," *Adv. Energy Mater.*, vol. 12, no. 2, Jan. 2022, Art. no. 2103249.

[11] I. Park, J. Maeng, D. Lim, M. Shim, J. Jeong, and C. Kim, "A 4.5-to-16μW integrated triboelectric energy-harvesting system based on high-voltage dual-input buck converter with MPPT and 70V maximum input voltage," in *IEEE Int. Solid-State Circuits Conf. (ISSCC) Dig. Tech. Papers*, vol. 50, Feb. 2018, pp. 146–148.

[12] I. Park, J. Maeng, M. Shim, J. Jeong, and C. Kim, "A high-voltage dual-input buck converter achieving 52.9% maximum end-to-end efficiency for triboelectric energy-harvesting applications," *IEEE J. Solid-State Circuits*, vol. 55, no. 5, pp. 1324–1336, May 2020.

[13] J. Maeng, I. Park, M. Shim, J. Jeong, and C. Kim, "A high-voltage dual-input buck converter with bidirectional inductor current for triboelectric energy-harvesting applications," *IEEE J. Solid-State Circuits*, vol. 56, no. 2, pp. 541–553, Feb. 2021.

[14] Y. Su, M. Yanagisawa, and Y. Shi, "A dual-output rectifier-based self-powered interface circuit for triboelectric nanogenerators," *IEEE Trans. Power Electron.*, vol. 39, no. 6, pp. 6630–6634, Jun. 2024.

[15] S. Xu, L. Zhang, W. Ding, H. Guo, X. Wang, and Z. L. Wang, "Self-doubled-rectification of triboelectric nanogenerator," *Nano Energy*, vol. 66, Dec. 2019, Art. no. 104165.

[16] A. Ghaffarinejad et al., "A conditioning circuit with exponential enhancement of output energy for triboelectric nanogenerator," *Nano Energy*, vol. 51, pp. 173–184, Sep. 2018.

[17] H. Zhang, F. Marty, D. Galayko, N. Hodzic, and P. Basset, "High-voltage MEMS plasma switch for boosting the energy transfer efficiency in triboelectric nanogenerators," in *Proc. IEEE 33rd Int. Conf. Micro Electro Mech. Syst. (MEMS)*, Jan. 2020, pp. 610–613.

[18] Y. Zhou, P. Zhang, J. Li, and X. Mao, "Recent progress of triboelectric nanogenerator-based power management and information processing circuit," *Mater. Today Sustainability*, vol. 23, Sep. 2023, Art. no. 100426.

[19] I. Kara, M. Becermis, M. A. Kamar, M. Aktan, H. Dogan, and S. Mutlu, "A 70-to-2 v triboelectric energy harvesting system utilizing parallel-SSHI rectifier and DC–DC converters," *IEEE Trans. Circuits Syst. I, Reg. Papers*, vol. 68, no. 1, pp. 210–223, Jan. 2021.

[20] M. Pathak and R. Kumar, "Synchronous inductor switched energy extraction circuits for triboelectric nanogenerator," *IEEE Access*, vol. 9, pp. 76938–76954, 2021.

[21] J. Lee, S.-H. Lee, G.-G. Kang, J.-H. Kim, G.-H. Cho, and H.-S. Kim, "A triboelectric energy-harvesting interface with scalable multi-chip-stacked bias-flip and daisy-chained synchronous signaling techniques," *IEEE J. Solid-State Circuits*, vol. 57, no. 12, pp. 3825–3839, Dec. 2022.

[22] S.-H. Lee, Y.-W. Jeong, S.-J. Park, and S.-U. Shin, "A rectifier-reusing bias-flip energy harvesting interface circuit with adaptively reconfigurable SC converter for wind-driven triboelectric nanogenerator," *IEEE Trans. Ind. Electron.*, vol. 70, no. 8, pp. 8022–8031, Aug. 2023.

[23] W. Peng, X. Yue, W. van Driel, G. Zhang, and S. Du, "A 70-V fully integrated dual-SSHC rectifier for triboelectric energy harvesting with full-digital duty-cycle-based MPPT achieving 598% power extraction enhancement," in *Proc. IEEE Custom Integr. Circuits Conf. (CICC)*, Apr. 2024, pp. 1–2.

[24] Z. Chen, M.-K. Law, P.-I. Mak, W.-H. Ki, and R. P. Martins, "Fully integrated inductor-less flipping-capacitor rectifier for piezoelectric energy harvesting," *IEEE J. Solid-State Circuits*, vol. 52, no. 12, pp. 3168–3180, Dec. 2017.

[25] S. Du, Y. Jia, C. Zhao, G. A. J. Amaratunga, and A. A. Seshia, "A fully integrated split-electrode SSHC rectifier for piezoelectric energy harvesting," *IEEE J. Solid-State Circuits*, vol. 54, no. 6, pp. 1733–1743, Jun. 2019.

[26] Z. Chen, M.-K. Law, P.-I. Mak, X. Zeng, and R. P. Martins, "Piezoelectric energy-harvesting interface using split-phase flipping-capacitor rectifier with capacitor reuse for input power adaptation," *IEEE J. Solid-State Circuits*, vol. 55, no. 8, pp. 2106–2117, Aug. 2020.

[27] W. Peng, X. Yue, L. Pakula, and S. Du, "31.11 A capacitor-based bias-flip rectifier with electrostatic charge boosting for triboelectric energy harvesting achieving auto-MPPT at breakdown voltage and 14× power extraction improvement," in *IEEE Int. Solid-State Circuits Conf. (ISSCC) Dig. Tech. Papers*, Feb. 2024, pp. 516–518.

[28] S. Stanzione, C. van Liempd, R. van Schaijk, Y. Naito, F. Yazicioglu, and C. Van Hoof, "A high voltage self-biased integrated DC–DC buck converter with fully analog MPPT algorithm for electrostatic energy harvesters," *IEEE J. Solid-State Circuits*, vol. 48, no. 12, pp. 3002–3010, Dec. 2013.

[29] S. Stanzione, C. van Liempd, M. Nabeto, F. R. Yazicioglu, and C. Van Hoof, "20.8 A 500nW batteryless integrated electrostatic energy harvester interface based on a DC–DC converter with 60V maximum input voltage and operating from 1μW available power, including MPPT and cold start," in *IEEE Int. Solid-State Circuits Conf. (ISSCC) Dig. Tech. Papers*, Feb. 2015, pp. 1–3.

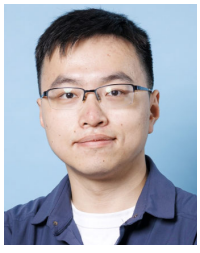

Wenyu Peng (Graduate Student Member, IEEE) received the B.Sc. degree from the Glasgow College, University of Electronic Science and Technology of China (UESTC), Chengdu, China, in 2020, and the M.Sc. degree in electronic instrumentation section from the Department of Microelectronics, Delft University of Technology (TU Delft), Delft, The Netherlands, in February 2023, where he is currently pursuing the Ph.D. degree with the Department of Microelectronics.

His current research interests include triboelectric and multisource energy harvesting for wearable, biomedical and IoT autonomous sensors, including energy-efficient power management circuit designs, and front-end harvester fabrications.

Xinling Yue (Graduate Student Member, IEEE) is currently pursuing the Ph.D. degree in microelectronics with the Electronic Instrumentation Laboratory, Delft University of Technology, Delft, The Netherlands.

She joined the Electronic Instrumentation Laboratory, Delft University of Technology, in December 2020. Her current research interests are energy-efficient power management integrated circuits and systems, which include energy harvesting, ac/dc rectifiers, dc/dc converters, and maximum power point tracking techniques.

Ms. Yue received the Best Student Paper Award at the 2022 IEEE International Conference on Electronics Circuits and Systems (ICECS), the Student Travel Grant Awards at the 2022 IEEE International Symposium on Circuits and Systems (ISCAS), the 2023 ISSCC and the 2023-2024 SSCS Predoctoral Achievement Award.

Willem D. van Driel received the degree in mechanical engineering from the Technical University of Eindhoven, Eindhoven, The Netherlands, and the Ph.D. degree from Delft University of Technology, Delft, The Netherlands.

He has more than 30 years of track record in the reliability domain. Application areas range from healthcare, gas and oil explorations, semiconductors. He is currently a Fellow Scientist with Signify (formerly Philips Lighting), The Netherlands. He is also a Professor at Delft University of Technology. He has authored and co-authored more than 400 scientific publications, including journal and conference papers, book or book chapters, and invited keynote lectures. His scientific interests are solid-state lighting, microelectronics and microsystems technologies, virtual prototyping, virtual reliability qualification, and designing for reliability of microelectronics and microsystems.

Dr. Driel is the Chair of the Organizing Committee of the IEEE Conference EuroSimE.

Guoqi Zhang (Fellow, IEEE) is a Member of Netherlands Academy of Engineering and the Chair Professor of "Micro/Nanoelectronics System Integration and Reliability," Delft University of Technology (TU Delft), Delft, The Netherlands. Before joining TU Delft, he worked at NXP and Philips, The Netherlands, as the Senior Director of technology strategy and a Research Fellow until 2013. His research interests cover multilevel heterogeneous system integration and packaging, multiphysics and multiscale modeling and optimization of micro/nanoelectronics, digital twin and designing for reliability, wide bandgap semiconductors sensors and components, and SSL technology.

Dr. Zhang received the IEEE Technical Field Award on packaging. He is currently serves as the Secretary-General for IEEE International Technology Roadmap of Wide bandgap power semiconductors (ITRW). He was the Chair of the "More than Moore" Team of European's Technology Platform for Micro/Nanoelectronics and served as the Co-Chair for the Academic Council of Dutch National Innovation Program on Micro/Nanoelectronics and Embedded System. He was the Founding Person for MEMSLand and the NL National MEMS Research Consortium.

Sijun Du (Senior Member, IEEE) received the B.Eng. degree (Hons.) in electrical engineering from the University Pierre and Marie Curie (UPMC), Paris, France, in 2011, the M.Sc. degree (Hons.) in electrical and electronic engineering from Imperial College, London, U.K., in 2012, and the Ph.D. degree in electrical engineering from the University of Cambridge, Cambridge, U.K., in January 2018.

He was with the Laboratoire d'Informatique de Paris 6 (LIP6), University Pierre and Marie Curie, and then worked as an IC Engineer in Shanghai, China, from 2012 to 2014. He was a Summer Engineer Intern at Qualcomm Technology Inc., San Diego, CA, USA., in 2016. He was a Post-Doctoral Researcher at the Department of Electrical Engineering and Computer Sciences (EECS), University of California at Berkeley, Berkeley, CA, USA., from 2018 to 2020. In 2020, he joined the Department of Microelectronics, Delft University of Technology (TU Delft), Delft, The Netherlands, as an Assistant Professor. His current research interests include energy-efficient integrated circuits and systems, including power management integrated circuits (PMIC), energy harvesting, wireless power transfer, and dc/dc converters used in IoT wireless sensors, wearable electronics, and biomedical devices.

Dr. Du received the Dutch Research Council (NWO) Talent Program VENI Grant in the 2021 round. He was a co-recipient of the Best Student Paper Award in IEEE ICECS 2022. He serves as the IEEE ICECS Sub-Committee Chair in 2022 and 2024, an IEEE ISSCC Student Research Preview (SRP) Committee Member since 2023, and the IEEE ISCAS Sub-Committee Chair in 2025.